JOURNAL OF SOLID STATE CHEMISTRY **136,** 21–33 (1998)
ARTICLE NO. SC977636

Neutron and X-Ray Powder Diffraction Study of $R\mathrm{Ba_2Fe_3O_{8+w}}$ Phases

P. Karen,* A. Kjekshus,* Q. Huang,†,‡ J. W. Lynn,‡ N. Rosov,‡ I. Natali Sora,‡,[1] V. L. Karen,‡ A. D. Mighell,‡ and A. Santoro‡

*Department of Chemistry, University of Oslo, Blindern, N-0315 Oslo, Norway; †University of Maryland, College Park, Maryland 20742; and ‡Reactor Radiation Division, National Institute of Standards and Technology, Gaithersburg, Maryland 20899

Received July 18, 1997; accepted September 22, 1997

Compounds of composition $R\mathrm{Ba_2Fe_3O_{8+w}}$ (R = La, Nd, Sm, Gd, Dy, Er, Yb, Lu, and Y) with variable oxygen content have been synthesized using the liquid mixing technique and have been analyzed by powder X-ray and neutron diffraction methods. A triple perovskite-type structure with ordered Ba and R cations and having the symmetry of space group $P4/mmm$ was obtained only for R = Y, Dy, and Er, whereas the larger R atoms gave the atomic arrangement of disordered, defective perovskites with average symmetry $Pm\bar{3}m$. No perovskite-type phases were obtained when Yb and Lu were tried. The oxygen content of the oxygen-saturated phases was found to increase with increasing size of the cation R from $w = 0.07$ for Er to $w = 0.83$ for La. The Néel temperature (~ 650 K) and the magnitude of the Fe magnetic moment ($\sim 3.3\ \mu_B$ at room temperature) are highest when trivalent iron is involved ($w = 0$), but these quantities are rather insensitive to the nature of R and to slight variations of oxygen content in the triple perovskite-type structure of the Y, Dy, and Er compounds. In the case of the cubic structures, however, both quantities depend strongly on the oxygen stoichiometry. In the magnetically ordered state, nearest-neighbor iron moments are coupled antiferromagnetically along the three crystallographic directions in all samples, resulting in magnetic structures with symmetry $Imm'm$ and magnetic unit cells related to those of the corresponding nuclear structures by the transformation matrix ($1\bar{1}0/110/002$).

INTRODUCTION

The nuclear and magnetic structures of $\mathrm{YBa_2Fe_3O_{8+w}}$ have been investigated by neutron powder diffraction for a composition corresponding to $w \simeq 0$ (1). The configuration of the atoms in the unit cell was found to have the symmetry of space group $P4/mmm$ and to be similar to that of the 123 superconductor $\mathrm{YBa_2Cu_3O_7}$, with the exception that the iron ions corresponding to the chain copper ions have distorted octahedral coordination, resulting in an oxygen stoichiometry of about eight atoms per formula unit. Bond length–bond strength calculations (1), according to Brown and Altermatt (2), based on the observed Fe–O distances, showed values of $+3.09$ and $+2.75$ for the valences of the octahedral and pyramidal iron cations, respectively.

The magnetic reflections observed in $\mathrm{YBa_2Fe_3O_{8+w}}$ were indexed in terms of a unit cell related to that of the nuclear structure by the transformation matrix ($1\bar{1}0/110/002$) and were consistent with a magnetic structure of symmetry $Imm'm$ in which the iron moments lie in planes perpendicular to the c-axis and are coupled antiferromagnetically within each ($\mathrm{FeO_2}$) layer as well as along the c-axis. The magnetic moments of the two crystallographically distinct iron cations were found to be the same within the experimental error of measurement.

In a subsequent study of $\mathrm{YBa_2Fe_3O_8}$, the foregoing results were corroborated by magnetic susceptibility, Mössbauer spectroscopy, and X-ray powder diffraction (3). From a fitting of Mössbauer data, however, Yuen *et al.* (4) suggested that the electronic valence states and the magnetic moments of the Fe ions at the two distinct sites are different, although the authors did not give specific values of the magnitude of the two individual moments.

The oxygen stoichiometry of $\mathrm{YBa_2Fe_3O_{8+w}}$ can be varied, but the amount of oxygen in excess of eight atoms per formula unit is generally very small, and even for the oxygen-saturated phase the value of w is only about 0.1 (5). Structural studies of the substitution phase $(\mathrm{Y_{1-x}Ca_x})\mathrm{Ba_2Fe_3O_{8+w}}$ have shown that the extra oxygen is located on the layer of the Y cations (6).

The Y ions of the 123 copper superconductor can be replaced by most of the rare earth elements without drastic changes of the structure and, in particular, without affecting the chemical ordering of the rare earth and barium cations (7) (in the case of the Nd, Pr, and La phases, however, the presence of these cations in the Ba sites has been reported (8)). This, however, does not seem to be the case for the iron compounds, in spite of structural similarities between the two systems. A triple perovskite-type structure has been reported when Y is replaced by Pr (4, 9), Eu (3), Dy, and Ho (10) although the reported symmetry of the Pr and Eu

[1]Present address: Department of Materials Chemistry and Physics, University of Brescia, 25123 Brescia, Italy.

0022-4596/98 $25.00

phases is doubtful. Pseudocubic perovskite-related superstructures have been observed in the case of Nd, Sm (11), and Gd (12). X-ray powder diffraction, electron diffraction, and high-resolution electron microscopy show that no ordering of the Ba and rare earth cations occurs in these superstructures and that the complexity of the stacking sequences of the iron coordination polyhedra along one of the pseudocubic axes is a function of the particular rare earth involved and of the oxygen stoichiometry of the material (11, 12). Clearly, preparation conditions with respect to temperature and partial pressure of oxygen play an important role in determining the structural features of these iron compounds.

In the present work, a number of $RBa_2Fe_3O_{8+w}$[2] materials (R = La, Nd, Sm, Gd, Dy, Er, Yb, Lu, and Y) with different oxygen stoichiometries have been synthesized with the same preparation techniques. The resulting materials have been analyzed by X-ray and neutron powder diffraction methods to establish which of the rare earths considered produce the $YBa_2Fe_3O_{8+w}$-type structure and which ones give cubic or pseudocubic type structures. Except for Sm and Gd, neutron diffraction has been used to provide the precise structural and magnetic parameters essential for an understanding of the similarities and differences between the copper and iron systems.

EXPERIMENTAL

A. Syntheses and Characterizations

Bulk synthesis. The samples used in this study were prepared by firing precursor materials obtained from liquid citrates. High-purity rare earth oxides La_2O_3, Nd_2O_3, Gd_2O_3, Er_2O_3, Sm_2O_3, Dy_2O_3, Y_2O_3, Yb_2O_3, and Lu_2O_3 were first standardized by high-temperature annealing and then dissolved in boiling critic acid monohydrate (50 mol of acid per mole of R_2O_3). After the solution was cooled, an equal volume of water was added and $BaCO_3$ was dissolved in the mixture. The iron component was added as a solution obtained by reaction of Fe powder, suspended in 10 times the weight of water, with nitric acid added drop by drop. The resulting solution was evaporated into a viscous melt, which was then dehydrated at 180°C into a brown solid, milled, and incinerated in air at 450°C. The amorphous precursor thus obtained was pressed into pellets and fired four times in an atmosphere of flowing O_2 at 1000°C for 100 hr, with intermittent rehomogenizations done by milling in a vibrating agate mill.

Oxygen pressure control. Partial pressures of oxygen $p_{O_2} > 10^{-4}$ atm were obtained by mixing Ar and O_2; lower p_{O_2}'s were controlled by the high-temperature equilibrium occurring in premixed argon, hydrogen (5 N purity), and water vapor. The latter was introduced from a $\sim$42.5 wt% solution of H_3PO_4 at room temperature, and the partial pressure of of $p_{H_2O} \approx 0.02$ atm was corrected for the actual temperature and concentration of H_3PO_4 in the saturator. The high-temperature composition of the gas was calculated from the dilution ratios and the thermodynamic data (13, 14) for the H_2O formation.

Oxygen content control. The equilibrium oxygen content in the solid oxide was controlled by the p_{O_2}, and temperature equilibria were controlled with the gas atmosphere. Three series were synthesized: (i) Oxygen-saturated samples across the array of selected R, obtained when the last firing was followed by oxidation in flowing O_2 ($\sim$1 atm) at 450°C for 100 hr and slow cooling inside the furnance; (ii) samples reduced to contain exactly trivalent iron, obtained when the series across the array of selected R was annealed (all samples in parallel) at 900°C for 100 hr in an atmosphere of flowing Ar containing 0.135% of hydrogen and 1.8% of water vapor, followed by rapid cooling (5 min to reach a temperature of 300°C) in the same atmosphere; and (iii) samples with varied oxygen content, synthesized for R = La, which exhibits the largest span in the attainable oxygen contents. This series was obtained by quenching the samples from temperatures of 450 and 900°C at various partial pressures of oxygen. The quenching apparatus had a vertical tube furnace with a flowing atmosphere of a diluted, mixed gas and a massive brass flange on the bottom having a conical hollow with a counterflow of dry, high-purity Ar (<1 ppm O_2) and a common gas outlet placed between the quenching place and the furnace. The duration of the annealing was 4–8 days according to the temperature.

Oxygen content analyses. The oxygen content in all samples was determined cerimetrically. The dissolutions of the samples were carried out in glass ampoules sealed in an Ar atmosphere. The dissolution time at temperatures close to 100°C was some 5 min. When the sample was reduced (Fe^{2+}), the solution in 3 M HCl was titrated directly, with ferroin as an indicator. When the sample was oxidized, a specified amount of previously titrated Mohr's salt was added and the remaining excess of Fe^{2+} was determined. The overall iron contents in the samples were determined in parallel, after a complete reduction of all iron present into Fe^{2+} by $SnCl_2$.

X-Ray characterization. Phase purity, lattice symmetry, and unit-cell parameters were determined by X-ray powder diffraction with a Guinier–Hägg camera, using Cu$K\alpha_1$ radiation and Si as internal standard.

B. Powder Neutron Diffraction and Refinement of the Structures

The neutron powder diffraction measurements were made with the high-resolution powder diffractometer at the

[2] In this paper all formulas are written as triple perovskites to facilitate the comparison of their compositions.

TABLE 1
Collection of PND Intensity Data

Monochromatic beam	311 reflection of a Cu monochromator
Wavelength	1.5396 Å
Horizontal divergences	15′, 20′, and 7′ of arc of the in-pile, monochromatic beam, and diffracted beam collimators, respectively
2θ angular range	3–163°, steps: 0.05°
Scattering amplitudes (10^{-12} cm)	b(La) = 0.827, b(Nd) = 0.769, b(Dy) = 1.69, b(Er) = 0.803, b(Y) = 0.775, b(Ba) = 0.525, b(Fe) = 0.954, b(O) = 0.581
Measured value of μ_{abs}	0.33 for R = Er and 0.75 for R = Dy

Reactor of the National Institute of Standards and Technology, using the experimental conditions listed in Table 1. The scans at 10 K were carried out to ascertain if nuclear and/or magnetic phase transitions take place at low temperature. The Gd- and Sm-containing materials were not analyzed by neutron diffraction because of the high absorption cross section of these elements for thermal neutrons. The intensities of the Dy and Er compounds were corrected for absorption using the measured transmission factors listed in Table 1. The structural refinements were carried out with the Rietveld method of profile analysis (15) using the program GSAS written by Larson and Von Dreele (16).

RESULTS

A. X-Ray Diffraction and Chemical Characterization

Table 2 shows the results of the X-ray and chemical characterization of the oxygen-saturated samples. For R = Yb and Lu, the reaction product was a mixture of phases, none being structurally related to perovskite. As shown in the table, only for R = Dy and Er (in addition to Y) was the triple perovskite-type configuration obtained. For R = La, Nd, Sm, and Gd the end products were cubic or pseudocubic phases giving X-ray diffraction patterns with sharp Bragg reflections in the case of La for $w = 0.8$ and broadened peaks in all other cases, indicating some disorder. The bulk samples were single phase, except for the Nd sample, which contained some 5% of a foreign phase, and the Er and Y samples, which contained about 1% of a (Ba, R)FeO$_3$, perovskite-type phase, occurring in the vicinity of the main phase in the phase diagram (17). The oxygen content increases significantly with increasing size of the R cation. Interestingly, the pseudocubic phases occur for large cations and may have large oxygen content, whereas not more than $w \simeq 0.1$ extra oxygen can be incorporated in the triple perovskite-type structure.

Table 3 shows the data obtained when all the phases are reduced to have an oxygen content of about eight atoms per formula unit. This is the stoichiometric composition for which the two crystallographically independent iron ions of the YBa$_2$Fe$_3$O$_8$-type structure have square-pyramidal and octahedral coordinations. It is somewhat surprising that none of the pseudocubic phases orders into the triple perovskite-type structure upon reduction, indicating that it is mainly the R, Ba ordering that controls the formation of the triple perovskite-type configuration. It is also interesting to note that the lattice parameters increase with decreasing oxygen content, showing that oxygen insertion in these compounds increases the oxidation state of iron with consequent contraction of its coordination polyhedra. Figure 1 shows the average perovskite parameters a_s (which is simply the parameter a for the cubic phases) plotted against the number of oxygen atoms per formula unit. Clearly, for any given oxygen content, the size of the unit cell in this series of compounds is determined by the radii of the R cations.

The data for bulk samples of LaBa$_2$Fe$_3$O$_{8+w}$ with different oxygen contents are listed in Table 4. In line with the other R variants, the oxygen content can also be reduced below $w = 0$. For the most electropositive R = La, the lowest partial pressures of oxygen are required. When the tolerance of the cubic LaBa$_2$Fe$_3$O$_{8+w}$ structure toward reduction is exceeded for $w < -0.20$ at 900°C, a dark green (an average Fe oxidation state +2.02) mixture of two phases is formed, one of which (some 10–20% of the

TABLE 2
Cerimetric Oxygen Content, Fe Valence v_{Fe}, and PXD Unit-Cell Parameters of Oxygen-Saturated RBa$_2$Fe$_3$O$_{8+w}$

R	$8+w$	v_{Fe}	a (Å)	c (Å)
La	8.80(2)	3.53	3.9431(2)	
Nd	8.48(1)	3.32	3.9374(4)	
Sm	8.31(1)	3.21	3.9375(4)	
Gd	8.17(1)	3.12	3.9328(5)	
Dy	8.09(1)	3.06	3.9198(5)	11.8162(19)
Y	8.09(1)	3.06	3.9167(4)	11.8126(16)
Er	8.07(1)	3.05	3.9140(4)	11.8013(16)

TABLE 3
Cerimetric Oxygen Content, Fe Valence v_{Fe}, and PXD Unit-Cell Parameters of "Stoichiometric" RBa$_2$Fe$_3$O$_{8+w}$ (w = 0.00(2))

R	$8+w$	v_{Fe}	a (Å)	c (Å)
La	8.017(5)	3.011	3.9924(4)	
Nd	7.995(5)	2.997	3.9598(3)	
Sm	7.994(5)	2.996	3.9529(6)	
Gd	7.989(5)	2.993	3.9416(5)	
Dy	7.988(5)	2.992	3.9220(3)	11.8255(15)
Y	7.987(5)	2.991	3.9173(4)	11.8194(16)
Er	7.984(5)	2.990	3.9152(4)	11.8129(18)

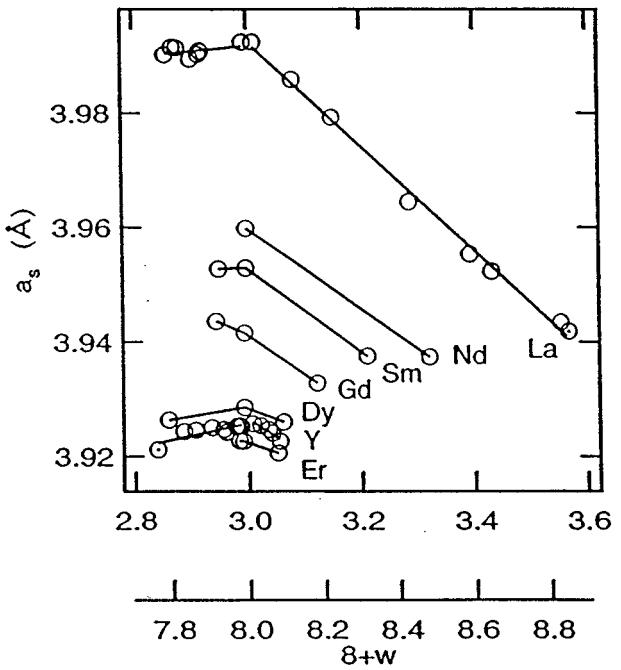

FIG. 1. Average single perovskite-type unit-cell parameter a_s (a for the cubic phases) as a function of the formal Fe valence and oxygen content of $R\mathrm{Ba_2Fe_3O_{8+w}}$. Standard errors do not exceed the size of the symbols.

sample) is cubic [$a = 3.952$ (4) Å] and the other hexagonal [$a = 11.8290(6)$ and $c = 7.1484(5)$ Å]. The hexagonal pattern bears some similarity to that calculated from the single-crystal structural data (18) for $\mathrm{Ba_6La_2Fe_4O_{15}}$.

TABLE 4
$\mathrm{LaBa_2Fe_3O_{8+w}}$ Bulk Sample with Varied Oxygen Content

$8 + w$	a (Å)	log p_{O_2}[a]	t (°C)
8.83(3)	3.9434(2)	0.0	450
8.65(4)	3.9523(3)	0.0	900
8.59(1)	3.9553(2)	−2.27(3)	450
8.22(1)	3.9792(4)	−2.17(4)	900
7.99(1)	3.9924(3)	−15.04(8)	900
7.88(1)	3.9909(4)	−17.06(9)	900

[a] Partial pressure of oxygen (in atm) from which the sample was quenched at the temperature t.

B. Nuclear and Magnetic Structure Refinements

In agreement with the X-ray results, the nuclear reflections in the neutron powder patterns of $R\mathrm{Ba_2Fe_3O_{8+w}}$ could be readily indexed assuming cubic symmetry in the case of R = La and Nd and triple perovskite-type cells in the case of R = Dy, Er, and Y. Whenever present, the magnetic reflections could be indexed in terms of magnetic unit cells related to those of the respective nuclear structures by the transformation matrix $(1\bar{1}0/110/002)$. In all cases (cubic and tetragonal structures), in the ordered state the contiguous iron moments were found to be coupled antiferromagnetically in all three crystallographic directions with spins lying in planes perpendicular to c_m. If we assume spins parallel to the a-axis, the resulting configuration is consistent with the symmetry of space group $Imm'm$.

TABLE 5
Refined Structural Parameters of the Oxygen-Saturated Cubic $R\mathrm{Ba_2Fe_3O_{8+w}}$, R = La ($w = 0.80$) and R = Nd ($w = 0.48$), at 296 and 10 K

				R = La		R = Nd	
				296 K	10 K	296 K	10 K
Nuclear unit cell: Space group $Pm\bar{3}m$							
			a (Å)	3.94280(3)	3.93494(4)	3.93613(4)	3.92816(4)
			V (Å^3)	61.293(1)	60.298(2)	60.983(2)	60.613(2)
R/Ba	1a	0, 0, 0	B (Å^2)	0.59(2)	0.29(2)	0.79(2)	0.44(2)
Fe	1b	$\frac{1}{2}, \frac{1}{2}, \frac{1}{2}$	B (Å^2)	0.44(2)	0.25(2)	0.53(2)	0.33(2)
O	3c	$0, \frac{1}{2}, \frac{1}{2}$	B_{11} (Å^2)	1.51(3)	1.14(2)	2.75(4)	2.43(4)
			B_{33} (Å^2)	0.79(3)	0.62(3)	0.97(5)	0.74(5)
			n	0.992(5)	0.988(5)	0.960(6)	0.947(6)
			$w = 9n - 8$	0.93(5)	0.89(5)	0.64(5)	0.52(5)
Magnetic unit cell[a]: Space group $Imm'm$							
			μ_{AF}[b] (μ_B)		1.25(2)		1.37(2)
R_p (%)				5.98	5.87	6.57	7.27
R_{wp} (%)				7.92	7.98	8.45	9.39
χ^2				1.23	1.24	1.45	1.51

[a] $a_m = b_m = \sqrt{2}a_n$; $c_m = 2a_n$.
[b] $\mu_{AF} = \mu_x$, $\mu_y = \mu_z = 0$.

TABLE 6
Refined Structural Parameters of the Oxygen-Saturated Cubic $LaBa_2Fe_3O_{8+w}$ at Room Temperature (First Line) and at 10 K (Second Line)

				$8+w^a$					
				8.83	8.65	8.59	8.22	7.99	7.88
Nuclear unit cell: Space group $Pm\bar{3}m$									
			a (Å)	3.94304(4)	3.95163(7)	3.95469(7)	3.9768(1)	3.9951(1)	3.98524(8)
				3.93380(4)	3.94335(6)	3.94582(7)	3.9681(1)	3.9874(1)	3.97693(7)
La/Ba	1*a*	0, 0, 0	B (Å^2)	0.51(1)	0.79(2)	0.83(2)	0.76(2)	1.33(3)	1.57(2)
				0.32(1)	0.48(2)	0.51(2)	0.41(3)	1.00(3)	1.18(2)
Fe	1*b*	$\frac{1}{2}, \frac{1}{2}, \frac{1}{2}$	B (Å^2)	0.44(1)	0.64(2)	0.69(2)	0.57(2)	1.19(3)	1.39(2)
				0.34(1)	0.41(2)	0.45(2)	0.34(3)	0.91(2)	1.13(2)
O	3*c*	$0, \frac{1}{2}, \frac{1}{2}$	B_{11} (Å^2)	1.37(2)	1.85(3)	2.00(3)	2.14(5)	2.58(5)	2.91(4)
				1.14(2)	1.49(3)	1.67(3)	1.87(3)	2.32(5)	2.62(3)
			B_{33} (Å^2)	0.76(2)	1.03(5)	1.08(5)	0.99(7)	0.95(7)	1.15(5)
				0.65(3)	0.89(4)	0.97(4)	0.75(6)	0.78(8)	0.89(4)
			n	0.987(4)	0.950(6)	0.944(5)	0.915(6)	0.849(6)	0.844(4)
				0.979(4)	0.950(5)	0.948(5)	0.921(7)	0.851(6)	0.845(4)
			$w = 9n - 8$	0.88(4)	0.55(5)	0.59(5)	0.24(5)	−0.36(5)	−0.40(4)
				0.81(4)	0.55(5)	0.53(5)	0.29(6)	−0.34(5)	−0.39(4)
Magnetic unit cell[b]: Space group $Imm'm$									
			μ_{AF} (μ_B)[c]		0.70(5)	0.50(5)	2.57(3)	3.53(3)	3.45(2)
				1.28	1.68(3)	1.63(3)	3.16(3)	3.89(3)	3.86(2)
R_p (%)				4.37	5.64	5.39	4.94	5.44	4.36
				4.84	5.98	5.65	5.34	5.85	4.53
R_{wp} (%)				5.64	7.34	6.91	6.43	6.80	5.48
				6.26	7.74	7.14	6.92	7.28	5.74
χ^2				1.40	2.44	1.69	1.60	1.36	1.69
				1.44	2.57	1.84	1.79	1.44	1.76

[a] By cerimetric analysis.
[b] $a_m = b_m = \sqrt{2}a_n$; $c_m = 2a_n$.
[c] $\mu_{AF} = \mu_x$, $\mu_y = \mu_z = 0$.

1. R = La and Nd. The cubic structures of the lanthanum and neodymium compounds were refined assuming the symmetry of space group $Pm\bar{3}m$ and the atomic arrangement of (cubic) perovskite, with the R and Ba cations disordered over the 1*a* site and with Fe and O in 1*b* and 3*c*, respectively. In all cases, the anisotropic temperature factors and the site occupancies of oxygen were refined together.

The structural refinements of the La and Nd compounds with low oxygen content were complicated by the presence of unsymmetrical tails on one side of the main Bragg peaks, suggesting a distribution of unit-cell dimensions. The problem was circumvented by assuming the presence of an additional cubic phase (about 5–10% of the sample) having a cell parameter slightly higher than that of the main phase and similar nuclear and magnetic structures. Due to the small amounts of the extra phase, in the course of the refinement only the lattice parameter could be varied, while occupancy and temperature factors of the oxygen were kept fixed at the values of those of the main phase. The ordering temperature and the magnitude of the iron magnetic moments were found to be a function of the oxygen content, and the highest value of the moment was obtained for $w \simeq 0$ ($\mu_{AF} = 3.89\ \mu_B$ at 10 K).

The refined structural parameters for the La and Nd oxygen-saturated phases are listed in Table 5, and in Table 6 are shown the results at 10 K for the various oxygen compositions of $LaBa_2Fe_3O_{8+w}$. An example of the agreement between observed and calculated intensities obtained for the La phase is shown in Figs. 2 and 3 for the 296 and 10 K experiments, respectively, and in Fig. 4, the nuclear and magnetic structures of the cubic phases are represented schematically. In Fig. 5 the magnitude of the magnetic moment at 10 and 296 K is plotted against the oxygen content of $LaBa_2Fe_3O_{8+w}$, and the magnetic order

parameter for the oxygen-saturated sample is plotted in Fig. 6.

2. R = Dy, Er, and Y. The structures of the Dy, Er, and Y compounds were refined assuming the space group $P4/mmm$ and the atomic configuration described in ref. 1 for $YBa_2Fe_3O_8$. In analogy with the results obtained for $(Y_{1-x}Ca_x)Ba_2Fe_3O_{8+w}$ (6), the oxygen in excess of eight atoms per formula unit was located on the layer of the R cations at $(0, 0, \frac{1}{2})$. The introduction of this extra oxygen in the structure produces a certain amount of disorder. More specifically, in those unit cells in which the sites $(0, 0, \frac{1}{2})$ are occupied, the oxygen atoms of the (FeO_2) layers located above and below the plane of the R atoms must be shifted toward the plane of the iron, not only to achieve reasonable O–O separations but also to provide as regular as possible an octahedral coordination for the iron cations. On the other hand, when the $(0, 0, \frac{1}{2})$ sites are vacant, as occurs in most cells in each crystallite, the oxygen atoms of the $\ldots(FeO_2)(R)(FeO_2)\ldots$ layers must be shifted away from the plane of the iron ions to ensure a stable fivefold coordination for Fe. For these reasons, the sites of the oxygen atoms associated with the pyramidally coordinated iron were split during the refinement along the direction of the c-axis, with the constraint that the number of atoms shifted must be equal to the number of the extra oxygen atoms located on the R layer. A further constraint was to assume that these atoms lie exactly on the plane of Fe, i.e., $z(O(2B)) = z(Fe(2))$, a situation that corresponds to an almost regular octahedron for the iron cations of the layers $\ldots(FeO_2)(RO_w)(FeO_2)\ldots$. This model was refined together with a magnetic structure assumed to be identical to that described in ref. 1 for $YBa_2Fe_3O_8$. The results of these calculations are listed in Table 7, and selected bond distances are listed in Table 8. An example of the agreement between observed and calculated intensities is shown in Fig. 7 for the Er compound at room temperature, and a schematic representation of the nuclear and magnetic structures (with labelling of the atoms) is illustrated in Fig. 8.

DISCUSSION

A. Structure

The temperature factors of oxygen atoms in the cubic structure of the La and Nd compounds are significantly anisotropic. The data in Table 5 show that the coefficients B_{11} and B_{22} are larger than B_{33} and that this anisotropy increases with decreasing oxygen content, i.e., with increasing

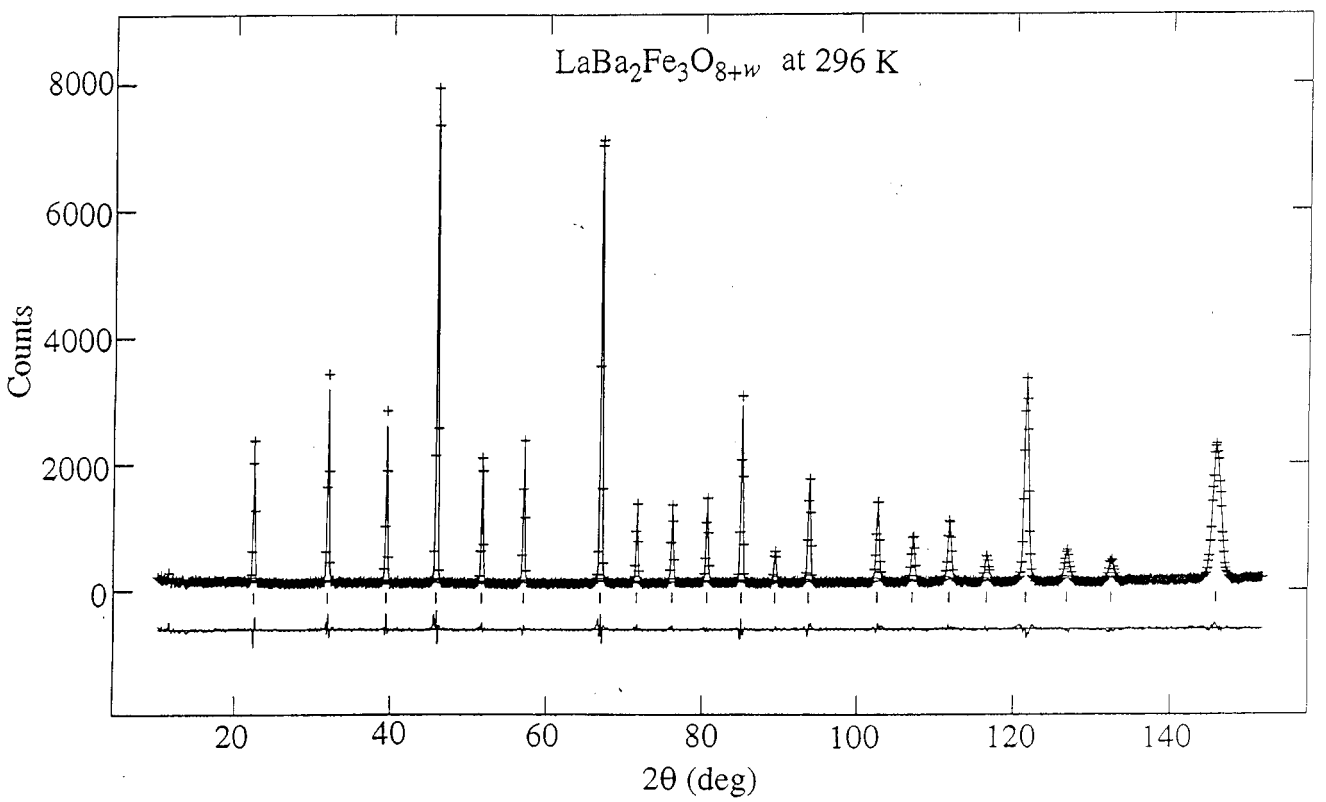

FIG. 2. Observed (crosses) and calculated (continuous line) intensities in the neutron powder pattern of cubic $LaBa_2Fe_3O_{8.80}$ at room temperature. The difference plot I(obs)–I(cal) is shown in the lower part of the figure. The short vertical lines indicate the Bragg angles at which reflections occur.

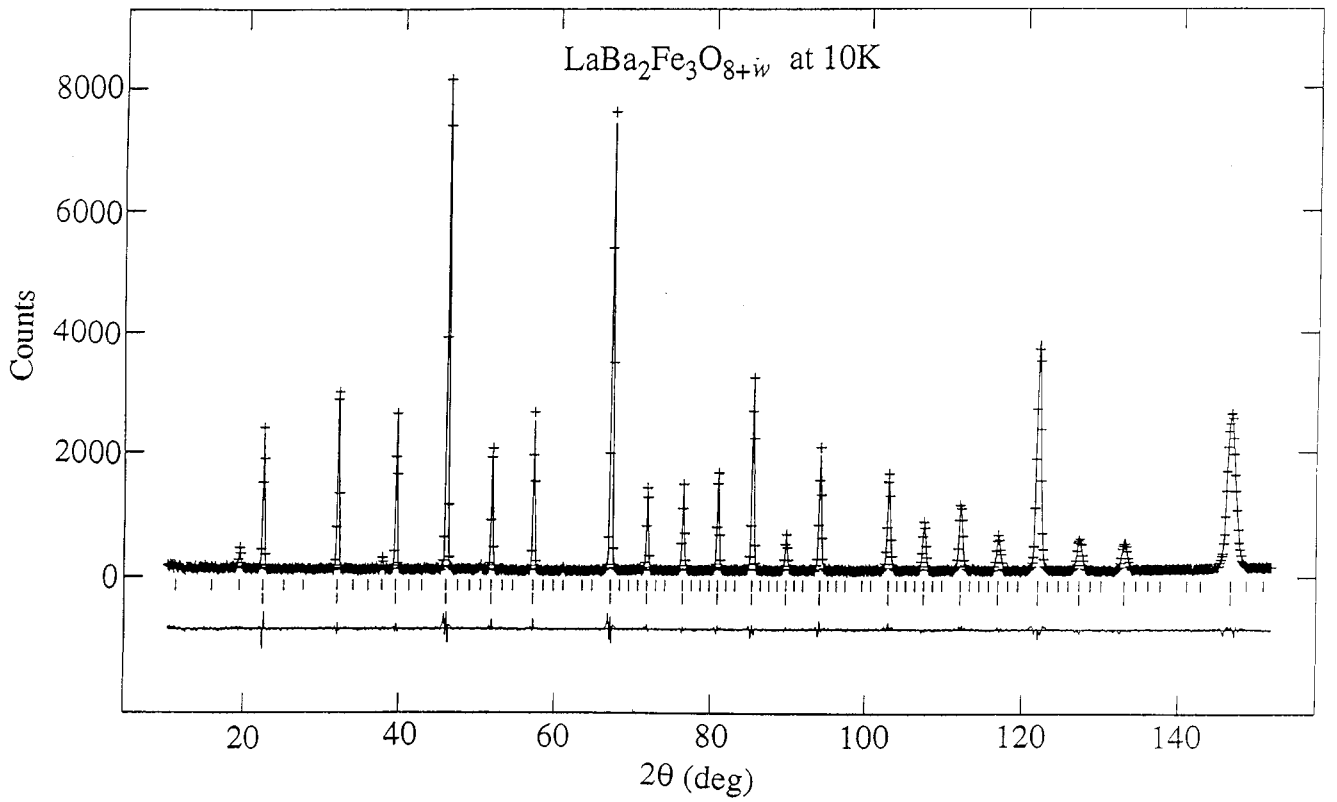

FIG. 3. Observed and calculated intensities in the neutron powder pattern of cubic $LaBa_2Fe_3O_{8.80}$ at 10 K. The short vertical lines in the first and second rows indicate the Bragg angles of the magnetic and nuclear reflections, respectively.

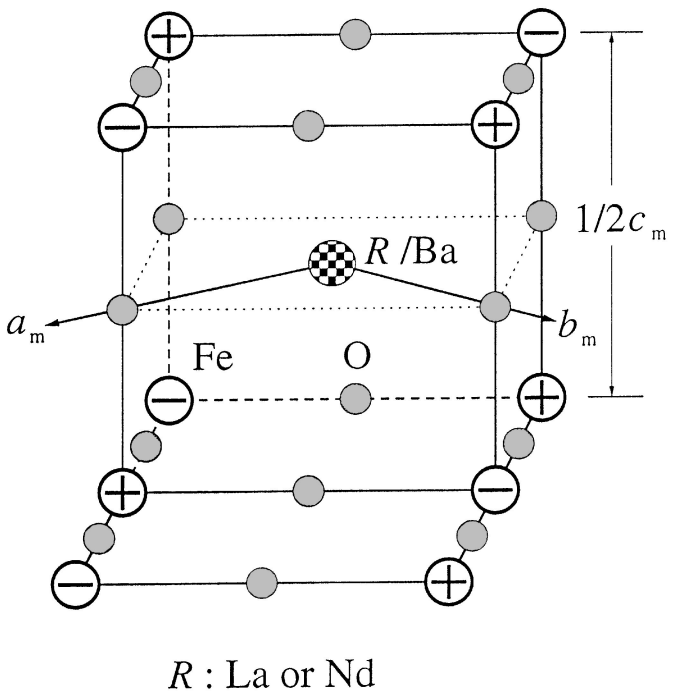

FIG. 4. Schematic representation of the nuclear and magnetic structures of cubic RBa$_2$Fe$_3$O$_{8+w}$. The plus and minus signs indicate the relative orientation of the Fe magnetic moments.

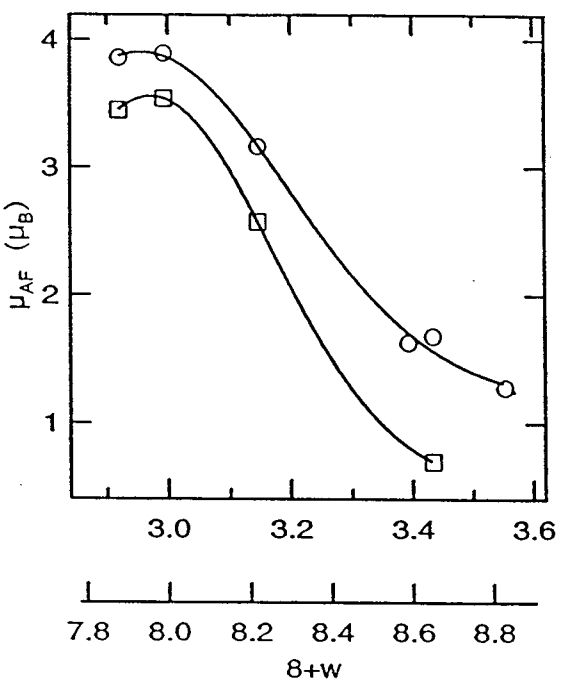

FIG. 5. Ordered magnetic moments at 10 K (circles) and at 296 K (squares) versus oxygen content and Fe valence in $LaBa_2Fe_3O_{8+w}$. Standard errors do not exceed the size of the symbols.

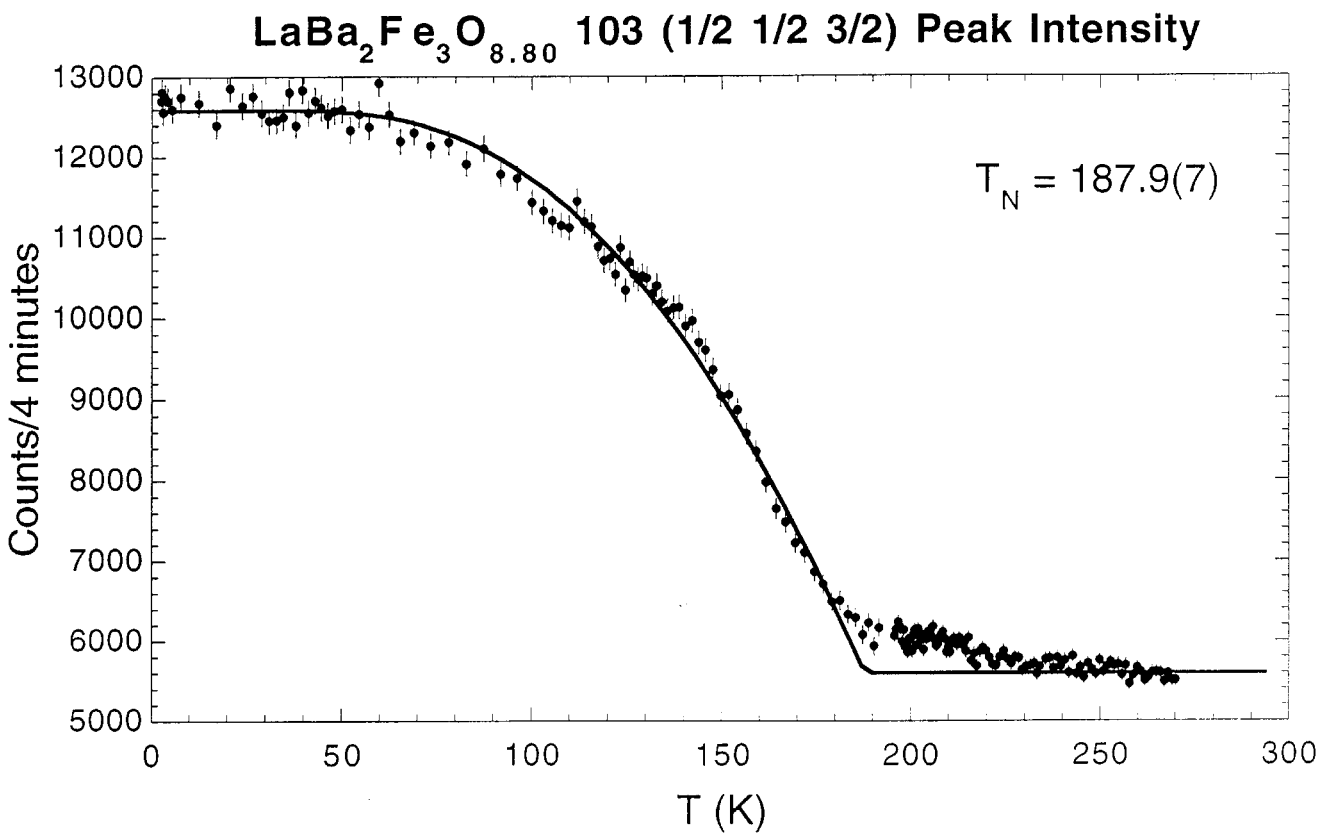

FIG. 6. Temperature variation of the intensity of the magnetic reflection 103 (nuclear $\frac{1}{2}, \frac{1}{2}, \frac{3}{2}$) for $LaBa_2Fe_3O_{8.80}$.

disorder in the structure. The fact that these parameters remain unusually large also at 10 K is a strong indication that some of the oxygen atoms may be shifted from the highly symmetrical positions they occupy in the perovskite-type structure. The nature of this disorder may be understood with the help of Fig. 9. The existence of an oxygen vacancy changes the coordination of the iron cation associated with it, from sixfold octahedral to fivefold pyramidal, and, as a consequence, a rearrangement of the oxygen atoms occurs (indicated by the arrows in Fig. 9) to ensure a more stable and regular coordination for the Fe cations.

In none of the neutron powder patterns of the La and Nd compounds were reflections observed that would indicate periodicities of the type shown by electron diffraction in similar systems (11, 12). This can be understood if one considers that a full ordering of the oxygen vacancies in these phases is possible for only a few specific values of the oxygen content parameters w. For all intermediate compositions, depending on the quenching procedure and oxygen content inhomogeneities, various stacking sequences of the iron coordination polyhedra may occur in different parts of each crystallite. The average structure revealed by the powder patterns, therefore, may well be cubic if this disorder occurs on a short-range level. Also, the appearance of tails on the low-2θ side of the main neutron peaks of these cubic compounds is evidence of disorder.

Since the Fe–O bond distances in the cubic compounds of La, Nd, Sm, and Gd are one-half the respective unit-cell parameters, their behavior as a function of oxygen content and radius of the rare earth cation is the same as that illustrated in Fig. 1 for a versus w. The Fe–O separations of $YBa_2Fe_3O_{8.09}$ (Table 8) are in generally good agreement with those reported previously for the stoichiometric composition (1). The data listed in Table 8 show that the bond distances for the tetragonal compounds do not change significantly in going from Dy to Y to Er and, in particular, the distortion of the $Fe(1)O_6$ octahedron and the configuration of the $Fe(2)O_5$ pyramid are the same for the three compounds. This is not surprising, considering that the ionic radii of the three R cations differ little from one another (1.027, 1.019, and 1.004 Å for Dy, Y, and Er, respectively) and that the oxygen stoichiometry is practically the same in the three cases ($w \simeq 0.08$). Bond length–bond strength calculations, based on the formalism and the parameters given by Breese and O'Keeffe (19), show a slight difference between the valence of the octahedral Fe(1) (3.02, 3.05, 3.03 valence

TABLE 7
Refined Structural Parameters of the Oxygen-Saturated Tetragonal $RBa_2Fe_3O_{8+w}$, R = Y ($w = 0.09$), R = Dy ($w = 0.09$), and R = Er ($w = 0.07$)

				R			
				Y (296 K)	Dy (296 K)	Er (296 K)	Er (10 K)
Nuclear unit cell: Space group P/mmm							
			a (Å)	3.91466(4)	3.91820(6)	3.91224(4)	3.90607(4)
			c (Å)	11.8156(2)	11.8165(3)	11.8047(2)	11.7679(3)
			V (Å^3)	181.72(1)	181.41(2)	180.678(6)	179.548(6)
R	1d	$\frac{1}{2}, \frac{1}{2}, \frac{1}{2}$	B (Å^2)	0.79(4)	0.81(3)	0.82(4)	0.36(4)
Ba	2h	$\frac{1}{2}, \frac{1}{2}, z$	z	0.1659(3)	0.1649(4)	0.1665(3)	0.1663(3)
			B (Å^2)	0.64(4)	0.72(6)	0.79(4)	0.42(4)
Fe(1)	1a	0, 0, 0	B (Å^2)	0.44(4)	0.58(5)	0.49(4)	0.15(4)
Fe(2)	2g	0, 0, z	z	0.3394(1)	0.3394(2)	0.3400(2)	0.3398(2)
			B (Å^2)	0.53(2)	0.69(3)	0.61(2)	0.37(2)
O(1)	2g	0, 0, z	z	0.1825(2)	0.1810(4)	0.1827(3)	0.1827(3)
			B (Å^2)	0.93(4)	1.29(6)	0.96(4)	0.55(4)
O(2A)	4i	0, $\frac{1}{2}$, z	z	0.3817(2)	0.3805(2)	0.3823(2)	0.3823(2)
			B (Å^2)	0.60(4)	0.69(5)	0.71(4)	0.49(4)
			n^a	0.941(5)	0.931(7)	0.956(6)	0.973(6)
O(2B)	4i	0, $\frac{1}{2}$, z	z^b	0.3394(1)	0.3394(2)	0.3400(2)	0.3398(2)
			B (Å^2)	0.60(4)	0.69(5)	0.71(4)	0.49(4)
			n	0.059(5)	0.069(7)	0.044(6)	0.027(6)
O(3)	2f	0, $\frac{1}{2}$, 0	B (Å^2)	0.74(4)	0.84(5)	0.79(4)	0.57(4)
O(4)	1b	0, 0, $\frac{1}{2}$	B (Å^2)^c	0.8	0.8	0.8	0.8
			n	0.059(5)	0.069(7)	0.044(6)	0.027(6)
			w	0.059(5)	0.069(7)	0.044(6)	0.027(6)
Magnetic unit cell^d: Space group $Imm'm$							
			μ_{AF} (μ_B)^e	3.43(3)	3.27(3)	3.41(2)	3.82(3)
R_p (%)				5.52	5.27	6.01	6.74
R_{wp} (%)				7.12	6.44	7.68	8.63
χ^2				1.32	1.11	1.22	1.22

[a] Occupancy factor constrained to $n_{O(2A)} = 1 - n_{O(2B)}$.
[b] Coordinate constrained to $z_{O(2B)} = z_{Fe(2)}$.
[c] Temperature factor fixed in the refinements.
[d] $a_m = b_m = \sqrt{2}a_n$; $c_m = 2a_n$.
[e] $\mu_{AF} = \mu_x$, $\mu_y = \mu_z = 0$.

units for the Y, Dy, and Er compounds, respectively) and the pyramidal Fe(2) (2.81, 2.79, and 2.79 valence units, respectively). These values are in good agreement with those reported in the previous publication (1) and are consistent with the deductions of Yuen *et al.* (4).

The data in Tables 2 and 3 show that the elements R that form the triple perovskite-type structure have ionic radii ranging from 1.004 (for Er) to 1.027 Å (for Dy) (20). For $r > 1.027$ Å, a disordered perovskite is obtained, while Yb and Lu ($r = 0.985$ and 0.977 Å, respectively), as mentioned earlier, form phase mixtures with non-perovskite-like structures. This behavior does not change by varying the method of preparation and the oxygen content of the samples. The literature for the cases of Pr (4, 9) and Eu (3) ($r = 1.126$ and 1.066 Å, respectively) seem to contradict this general trend. However, the X-ray powder patterns reported in refs 4 and 9 do not show the expected tetragonal splittings of some of the reflections. In particular, the reflections 200 and 006 (indexing based on the triple perovskite-type unit cell) seem to be exactly superposed (i.e., $c/a = 3.000$), indicating that the average symmetry of $PrBa_2Fe_3O_{8+w}$ is cubic rather than tetragonal. No powder pattern was reported for $EuBa_2Fe_3O_{8+w}$ in ref 3. Also in this case, however, the tetragonal symmetry is in question, since electron diffraction results (11) showed that the symmetry of this compound is pseudocubic.

The general behavior of the R substitution in the Fe phases is markedly different from that of the Cu phases,

TABLE 8
Selected Interatomic Distances (Å) in Oxygen-Saturated (See Table 7) Tetragonal $R Ba_2Fe_3O_{8+w}$

	Y (296 K)	Dy (296 K)	Er (296 K)	Er (10 K)
Fe(1)–O(1)	2.157(3)	2.138(4)	2.156(3)	2.150(4)
Fe(1)–O(3)	1.95734(2)	1.92910(2)	1.95612(2)	1.95304(2)
Fe(2)–O(1)	1.854(4)	1.873(5)	1.858(4)	1.848(4)
Fe(2)–O(2A)	2.0201(5)	2.0182(8)	2.0188(2)	2.0163(6)
Fe(2)–O(2B)	1.95734(2)	1.95910(2)	1.95612(2)	1.95304(2)
Fe(2)–O(4)	1.897(2)	1.897(2)	1.888(2)	1.886(2)
Ba–O(1)	2.7751(4)	2.7771(5)	2.7730(4)	2.7688(4)
Ba–O(2A)	3.215(3)	3.214(4)	3.212(4)	3.206(3)
Ba–O(2B)	2.835(3)	2.845(4)	2.833(3)	2.825(3)
Ba–O(3)	2.770(3)	2.763(3)	2.773(3)	2.765(3)
R–O(2A)	2.405(1)	2.415(2)	2.399(1)	2.394(1)
R–O(2B)	2.726(1)	2.727(2)	2.719(1)	2.715(1)
R–O(4)	2.76810(3)	2.77059(4)	2.76637(3)	2.76201(3)
O(2B)–O(1)	2.696(3)	2.710(4)	2.698(3)	2.689(3)
O(2B)–O(4)	2.726(1)	2.727(3)	2.719(2)	2.715(1)

where the substitution of Y by practically all rare earth elements does not modify the basic atomic arrangement of the triple perovskite-type structure of the 123 superconductor (7). This has something to do with the number and the arrangement of the oxygen vacancies at Cu(1) in relation to the stable oxidation states of copper. Iron can assume higher oxidation states, thus supporting more or less regular octahedral coordination at Fe(1). With the Fe(1) octahedron fully occupied, the population of oxygen on the *R* layers (and the stability of the triple perovskite-type structure) will depend critically on the size of the *R* cations. This can be understood by remembering that iron can be easily oxidized to states above +3, and oxygen can therefore be readily incorporated on the *R* layers with formation of pseudocubic structures of the type described in refs 10–12.

B. Fe Magnetism

Our results show that in the cubic structures of the La and Nd compounds the ordered moment of the iron cations increases with decreasing oxygen content. More specifically, in the case of $LaBa_2Fe_3O_{8+w}$, the moment at 10 K increases from 1.28 μ_B for $w = 0.83$ to 3.89 μ_B for $w = 0$ (Table 6).

The suppression of the ordered magnetic moment when the Fe valence departs from 3.00 can in principle have two causes: (i) All unpaired spins are AF-ordered (at low temperature), but their *number* decreases by the formation of low-spin iron owing to crystal-field effects. (ii) The *portion* of

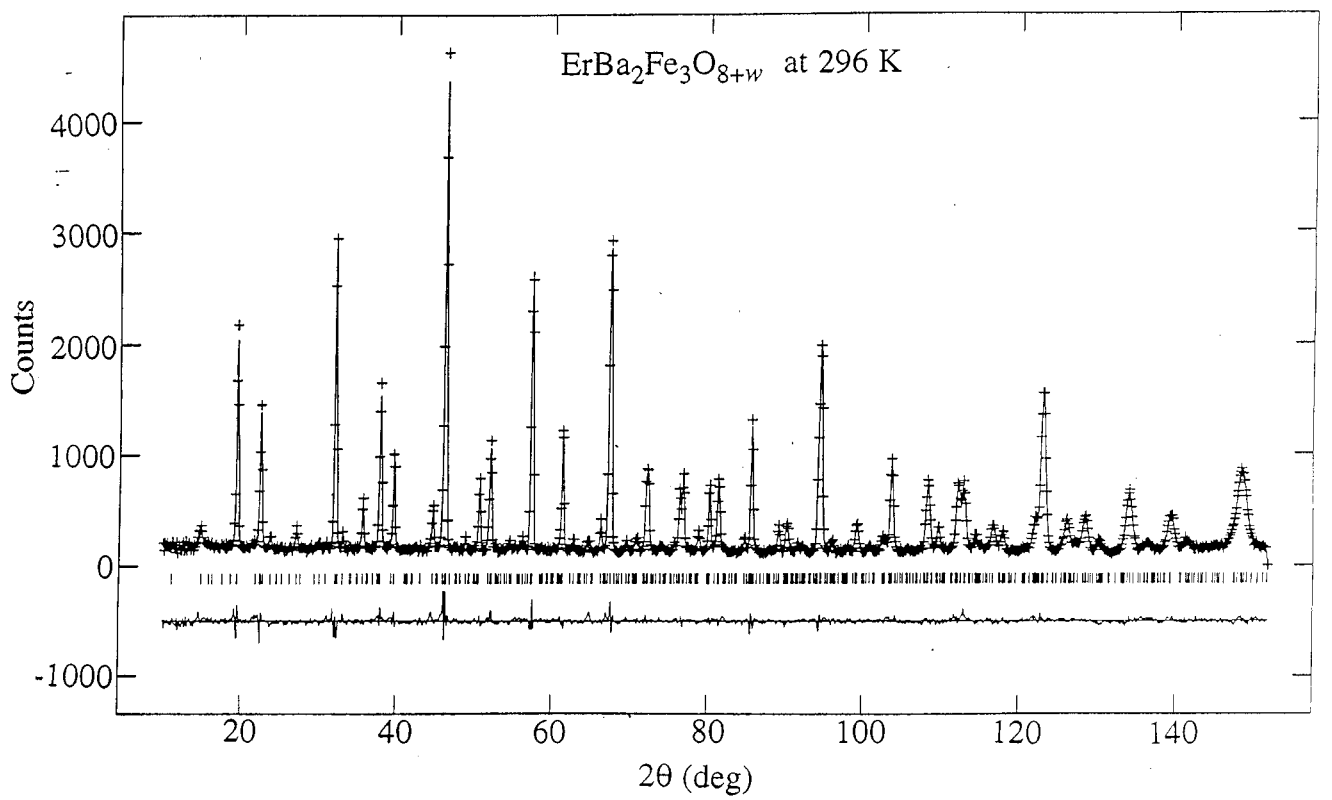

FIG. 7. Observed and calculated intensities in the neutron powder pattern of $ErBa_2Fe_3O_{8.07}$ at room temperature. The symbols are the same as those given in Fig. 2.

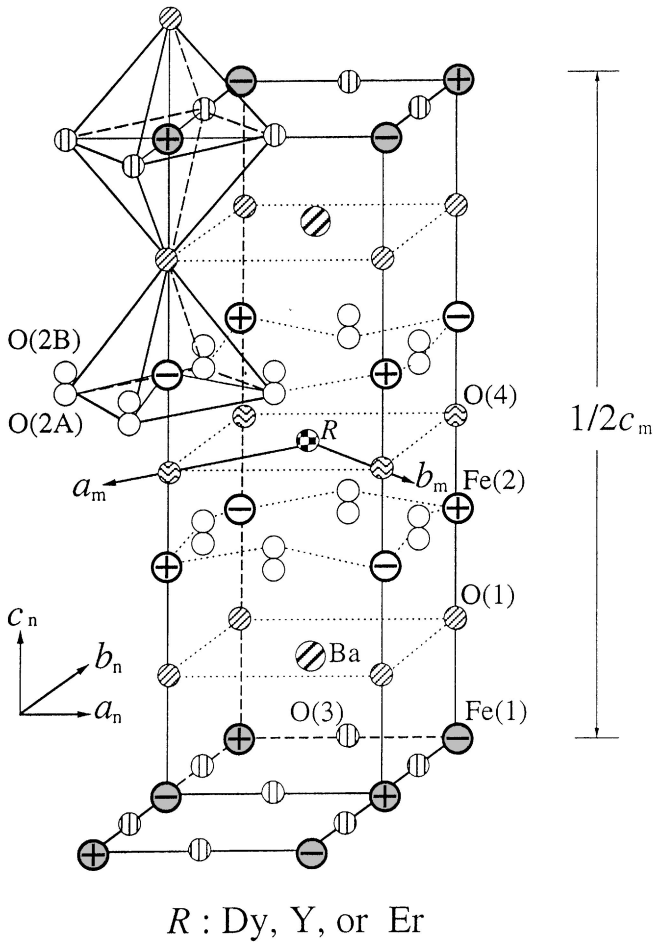

FIG. 8. Schematic representation of the nuclear and magnetic structures of the triple perovskite-type phases of Dy, Y, and Er. The ordering of the Fe magnetic moments is indicated with plus and minus signs. The moments lie on the a_m, b_m plane.

unpaired spins that is AF-ordered decreases (topological or dynamic fluctuations), owing to a disruption of the superexchange. According to a recent Mössbauer spectroscopy study (21), only high-spin states occur in LaBa$_2$Fe$_3$O$_{8+w}$, and therefore, some local magnetic disruption appears as the most likely cause. Such AF frustration can be of various kinds, introducing local ferromagnetic clusters via moments residing at the oxygen atoms and/or by the presence of another valence/spin Fe state at neighboring sites.

One such approach is chosen here to illustrate the point. According to the findings for Ba$_{1-x}$La$_x$FeO$_3$ (22, 23), it is assumed that disordered ferromagnetic defects are formed by Fe^{3+} and Fe^{5+} pairs, originating from a charge disproportionation of an average iron valence state $v+$:

$$Fe^{v+} \rightarrow \frac{5-v}{2} Fe^{3+} + \frac{v-3}{2} Fe^{5+} \qquad [1]$$

If, following ref 23, we assume (i) that such disproportionation occurs also in our La compound, (ii) that the ordered moment of the Fe^{3+} cation is about 4.0 μ_B and that of a Fe^{5+} cation about 2.5 μ_B, (iii) that the Fe^{3+} and Fe^{5+} cations are randomly distributed over the Fe sites, and (iv) that antiferromagnetic coupling occurs between Fe cations with the same charge and ferromagnetic coupling between those of different charges, then we may calculate the magnitude of the average magnetic moment at any site with the following procedure. In a perovskite structure, each Fe has six neighboring Fe ions forming an octahedral cage. If the central cation is Fe^{3+}, its moment will be $\{4(6-n) - 2.5n\}/6$, where n is the number of Fe^{5+} cations present in the surrounding cage (if the central cation is Fe^{5+}, the expression is the same, but with opposite sign ($\{2.5n - 4(6-n)\}/6$). Taking into consideration all possible cases and their probability of occurrence, the average magnitude of the magnetic moment of an iron ion is given by

$$\mu_{AF,av} = \left\{ \sum_{n=0}^{6} \left[\left(\frac{5-v}{2}\right)^{6-n} \left(\frac{v-3}{2}\right)^{n} \frac{6!}{(6-n)!\,n!} \times \frac{4(6-n) - 2.5n}{6} \right] \right\} \left\{ \frac{5-v}{2} - \frac{v-3}{2} \right\} \qquad [2]$$

The results of these calculations for LaBa$_2$Fe$_3$O$_{8+w}$ at 10 K are listed in Table 9 and show that the model adopted can account for the experimental results.

Attempts to refine separately the magnitudes of the ordered magnetic moments of Fe(1) and Fe(2) in the tetragonal structures were unsuccessful due to the high correlation between these two parameters, and for this reason the values shown in Table 7 were obtained by constraining the two moments to be the same. It should be pointed out that the results advanced in ref 4 maintain that the moments of Fe(1) and Fe(2) in YBa$_2$Fe$_3$O$_8$ are different

TABLE 9
Observed and Calculated Magnetic Moments of Fe for LaBa$_2$Fe$_3$O$_{8+w}$

			Fraction of Fe valence			
w	$v_{c.a.}$[a]	$v_{s.d.}$[a]	Fe^{3+}	Fe^{5+}	$\mu_{AF(obs)}$ (μ_B)	μ_{calc}[b] (μ_B)
0.80	+3.53	+3.46	0.735	0.265	1.28	1.08
0.65	+3.43	+3.34	0.785	0.215	1.68	1.48
0.59	+3.40	+3.31	0.800	0.200	1.63	1.62
0.22	+3.13	+3.15	0.935	0.065	3.16	3.11
−0.01	+3.00	+2.84	1.00	0.00	3.89	4.00
−0.12	+2.92	+2.83			3.86	

[a] $v_{c.a.}$: iron valence according to chemical analysis. $v_{s.d.}$: iron valence according to structure determination; bond length–bond strength calculation.

[b] Calculated from Eq. [2].

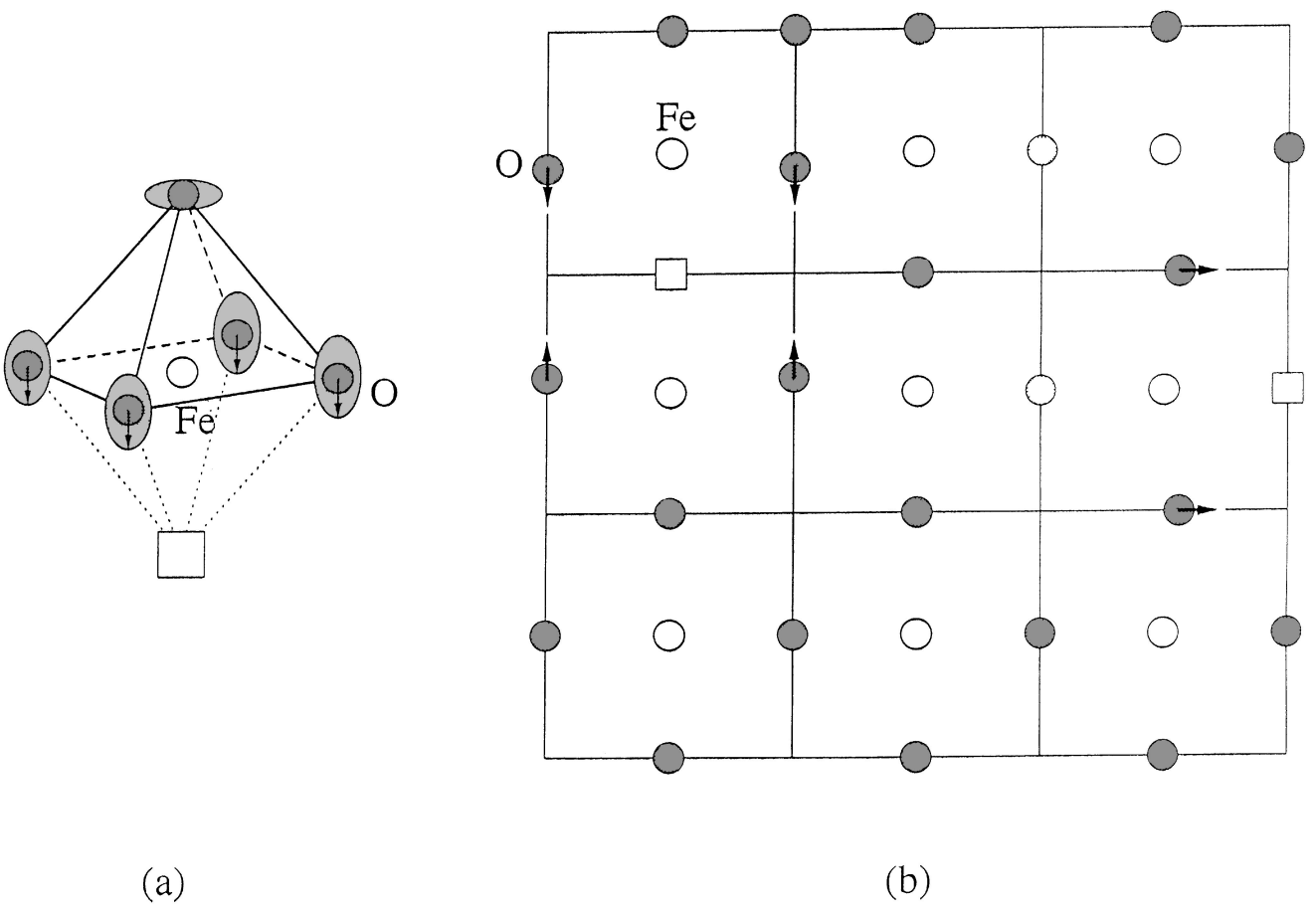

FIG. 9. Graphical interpretation of the atomic shifts in the La and Nd phases. (a) Oxygen vacancy present in an FeO_6 octahedron. The shifts of the oxygen atoms are indicated by arrows. (b) Projection of the defective octahedra perpendicularly to the O–Fe–□ vertical direction.

from each other, and we therefore merely conclude that this difference is too small to be detected in our neutron experiments.

As shown in Table 7, the values of the ordered magnetic moments in the Y, Dy, and Er compounds at room temperature are rather insensitive to the nature of the rare earth cation. This result and the almost constant values of the ordering (Néel) temperatures for these materials (about 650 K) show that replacement of Y by other rare earth elements does not have a significant effect on the magnetic properties in these triple perovskite-type phases. The only exception reported in the literature (Ref. 9) is $PrBa_2Fe_3O_{8+w}$, which has an ordering temperature of $T_N \simeq 230$ K and magnetic susceptibility anomalies at 23 and 55 K. As mentioned earlier, however, the Pr compound is cubic, rather than tetragonal, and should not be compared with triple perovskite-type structures.

The oxygen stoichiometry of the tetragonal structures of Y, Dy, and Er is close to $w = 0$, even in the oxygen-saturated samples, corresponding to an average iron valence of about $3+$. Not surprisingly, the magnitude of the average magnetic moment of iron in these compounds is high. In the case of Er, the moment at 10 K is 3.82 μ_B. The somewhat smaller values for Y, Dy, and Er at room temperature are presumably due to local thermal spin misalignments or other types of disordering.

In conclusion, we have determined the structures of $RBa_2Fe_3O_{8+w}$ (R = La, Nd, Sm, Gd, Dy, Er, and Y) by X-ray and/or neutron powder diffraction techniques. Only the Y, Dy, and Er phases have the triple perovskite-type structure. The others have cubic or pseudocubic configurations. The magnetic behavior of all phases (except Sm and Gd) has been analyzed. In the ordered state the nearest-neighbor iron moments are coupled antiferromagnetically along all three crystallographic directions.

Note added in proof. It should be noted that the occurrence of Fe^{5+}, assumed in deriving eq. (2), could not be confirmed by Mössbauer spectroscopy for any of the compounds studied (J. Linden, A. Kjekshus, P. Karen, J. Miettinen, and M. Karppinen, *J. Solid State Chem.*, submitted; see also Ref. (21)). However, the model calculations do not depend strongly on the Fe^{5+} hypothesis and give similar results when an oxidation state of Fe^{4+} is assumed.

REFERENCES

1. Q. Huang, P. Karen, V. L. Karen, A. Kjekshus, J. W. Lynn, A. D. Mighell, N. Rosov, and A. Santoro, *Phys. Rev. B* **45,** 9611 (1992).
2. I. D. Brown and D. Altermatt, *Acta Crystallogr. B* **41,** 244 (1985).
3. I. Felner, I. Nowik, U. Yaron, O. Cohen, E. R. Bauminger, T. Kroener, and G. Czjzek, *Phys. Rev. B* **48,** 16040 (1993).
4. T. Yuen, M. Seyedahmadian, R. E. Salomon, G. H. Myer, and G. Gao, *J. Appl. Phys.* **79,** 6001 (1996).
5. P. Karen and A. Kjekshus, *J. Solid State Chem.* **112**, 73 (1994).
6. I. Natali Sora, Q. Huang, J. W. Lynn, N. Rosov, P. Karen, A. Kjekshus, V. L. Karen, A. D. Mighell, and A. Santoro, *Phys. Rev. B* **49,** 3465 (1994).
7. Y. Le Page, T. Siegriest, S. A. Sunshine, L. F. Schneemeyer, D. W. Murphy, S. M. Zahurak, J. V. Waszczak, W. R. McKinnon, J. M. Tarascon, G. W. Hull, and L. H. Green, *Phys. Rev. B* **36,** 3617 (1987); M. Tarascon, W. R. McKinnon, L. H. Green, G. W. Hull, and E. M. Vogel, *Phys. Rev. B* **36,** 226 (1987).
8. P. Karen, H. Fjellvåg, O. Braaten, A. Kjekshus, and H. Bratsberg, *Acta Chem. Scand.* **44,** 994 (1990); M. Park, M. J. Kramer, K. W. Dennis, and R. W. McCallum, *Physica C* **259,** 43 (1996).
9. I. Felner, G. Hilscher, H. Michor, G. Wottmann, J. Dumschat, V. P. S. Awana, and S. K. Malik, *Phys. Rev. B* **54,** 11999 (1996).
10. E. García-González, M. Parras, J. M. González-Calbet, and M. Vallet-Regí, *J. Solid State Chem.* **104,** 232 (1993).
11. E. García-González, M. Parras, J. M. González-Calbet, and H. Vallet-Regí, *J. Solid State Chem.* **105,** 363 (1993).
12. E. García-González, M. Parras, J. M. González-Calbet, and M. Vallet-Regí, *J. Solid State Chem.* **110,** 142 (1994).
13. I. Barin and O. Knacke, "Thermochemical Properties of Inorganic Substances," pp. 316, 584. Springer-Verlag, New York, 1973.
14. I. Barin, O. Knacke, and O. Kubashevski, "Thermochemical Properties of Inorganic Substances, Supplement," p. 295. Springer-Verlag, New York, 1977.
15. H. M. Rietveld, *J. Appl. Crystallogr.* **2,** 65 (1969).
16. A. C. Larson and R. B. Von Dreele, "General Structure Analysis System," Los Alamos National Laboratory, Los Alamos, NM, 1990. [Report LA-UR-86-748]
17. P. Karen, P. H. Andresen, and A. Kjekshus, *J. Solid State Chem.* **101,** 48 (1992).
18. H. Mevs and H. Müller-Buschbaum, *J. Less-Common Met.* **157,** 173 (1990).
19. N. E. Breese and M. O'Keeffe, *Acta Crystallogr. B* **47,** 192 (1991).
20. R. D. Shannon, *Acta Crystallogr. A* **32,** 751 (1976).
21. J. Lindén, M. Lippmaa, A. Kjekshus, P. Karen, and M. Karppinen, *J. Solid State Chem.* [submitted for publication].
22. T. C. Gibb and M. Matsuo, *J. Solid State Chem.* **81,** 217 (1989).
23. P. D. Battle, T. C. Gibb, P. Lightfoot, and M. Matsuo, *J. Solid State Chem.* **85,** 38 (1990).